Journal of Computational Physics 444 (2021) 110573

Contents lists available at ScienceDirect

Journal of Computational Physics

www.elsevier.com/locate/jcp

An adaptive boundary element method for the transmission problem with hyperbolic metamaterials

Junshan Lin [1]

Department of Mathematics and Statistics, Auburn University, Auburn, AL 36849, United States of America

ARTICLE INFO

Article history:
Available online 26 July 2021

Keywords:
Hyperbolic metamaterials
Boundary element method
Adaptive algorithm
A posteriori error estimator

ABSTRACT

In this work we present an adaptive boundary-integral equation method for computing the electromagnetic response of wave interactions in hyperbolic metamaterials. The indefiniteness of the permittivity tensor gives rise to preferential wave radiation within the propagating cone for the hyperbolic media, and this induces sharp transition for the solution of the integral equation across the cone boundary when waves start to decay or grow exponentially. In order to avoid a global refined mesh over the whole boundary, we employ a two-level a posteriori error estimator and an adaptive mesh refinement procedure to resolve the singularity locally for the solution of the integral equation. Such an adaptive procedure allows for the reduction of the number of the degrees of freedom significantly for the integral equation solver while achieving desired accuracy for the solution. In addition, to resolve the fast transition of the fundamental solution and its derivatives accurately across the propagation cone boundary, adaptive numerical quadrature rules are applied to evaluate the integrals for the stiffness matrices. Finally, to formulate the integral equations over the boundary we also derive the limits of layer potentials and their derivatives in the hyperbolic media when the target points approach the boundary.

1. Introduction

1.1. Background

Hyperbolic metamaterials are a class of uniaxial anisotropic electromagnetic materials for which the axial principle component of their relative permittivity or permeability tensors attain opposite sign of the other two principal components:

$$\boldsymbol{\varepsilon}(x) = \begin{bmatrix} \varepsilon_{\parallel}(x) & 0 & 0 \\ 0 & \varepsilon_{\perp}(x) & 0 \\ 0 & 0 & \varepsilon_{\perp}(x) \end{bmatrix} \quad \text{or} \quad \boldsymbol{\mu}(x) = \begin{bmatrix} \mu_{\parallel}(x) & 0 & 0 \\ 0 & \mu_{\perp}(x) & 0 \\ 0 & 0 & \mu_{\perp}(x) \end{bmatrix}. \tag{1.1}$$

In the above, the subscripts $\parallel$ and $\perp$ denote the component parallel and perpendicular to the optical axis (oriented along the x_1 direction here) respectively, and it holds that

$$\mathrm{Re}\varepsilon_{\perp} \cdot \mathrm{Re}\varepsilon_{\parallel} < 0 \quad \text{or} \quad \mathrm{Re}\mu_{\perp} \cdot \mathrm{Re}\mu_{\parallel} < 0.$$

E-mail address: jzl0097@auburn.edu.

[1] Junshan Lin was partially supported by the NSF grant DMS-2011148.

https://doi.org/10.1016/j.jcp.2021.110573
0021-9991/

Hyperbolic metamaterials can be realized, for instance, by alternating metal–dielectric layers or by embedding metallic wire array in a dielectric matrix by restricting free-electron motion to certain directions [21,36,39]. The homogenized media will attain the anisotropy described by (1.1). More recently, hexagonal boron nitride (hBN), α-phase molybdenum trioxide (α-MoO_3), α-phase vanadium pentoxide (α-V_2O_5) and a few others have emerged as natural hyperbolic materials that attain opposite signs for the in-plane and out-of-plane components of the permittivity tensor [5,16,17,31,34,40]. These natural hyperbolic materials typically have layered structures, in which the optical axis is pointing out-of-plane and $\varepsilon_{\parallel}(x)$ in (1.1) refers to the out-of-the-plane component of the permittivity tensor.

Assume that the media is nonmagnetic such that the permeability reduces to the unit tensor, then the dispersion relation for the time-harmonic (with $e^{-i\omega t}$ dependence) Maxwell's equations

$$\nabla \times E = i\omega\mu_0\mu H, \quad \nabla \times H = -i\omega\varepsilon_0\varepsilon E$$

is given by

$$\left(k_1^2 + k_2^2 + k_3^2 - \varepsilon_{\perp} k_0^2\right) \cdot \left(\frac{k_1^2}{\varepsilon_{\perp}} + \frac{k_2^2 + k_3^2}{\varepsilon_{\parallel}} - k_0^2\right) = 0, \tag{1.2}$$

where ε_0 and μ_0 are the free-space permittivity or permeability, k_0 is the free-space wavenumber, and k_1, k_2 and k_3 are the x_1, x_2 and x_3 components of the wave vector respectively in the Cartesian coordinate. The first term in (1.2) corresponds a spherical isofrequency surface for the transverse electric (TE) polarized waves, while the second term gives rise to a hyperboloidal isofrequency surface for the transverse magnetic (TM) polarized waves when $\mathrm{Re}\varepsilon_{\perp} \cdot \mathrm{Re}\varepsilon_{\parallel} < 0$. It is seen that the TM waves remain propagating with arbitrarily large wave vectors in the hyperbolic medium, as opposed to evanescent in an isotropic medium. This unique property leads to many interesting applications of hyperbolic metamaterials ranging from sub-wavelength light manipulation and imaging to spontaneous and thermal emission modification [13,26,28,37,38].

1.2. Problem formulation

In this paper, we focus on the computation of the electromagnetic response from the wave interactions in hyperbolic metamaterials. We study the two-dimensional problem when the medium is invariant along the x_3 direction and the wave is TM-polarized with the magnetic field $H = (0, 0, u)^T$. The TE-polarized case is less interesting as it leads to an isotropic problem with the dispersion relation given by the first term of (1.2), and various existing computational methods can be applied to solve the problem. The Maxwell's equations in the hyperbolic medium for the TM-polarized polarization reduce to the scalar wave equation

$$\nabla \cdot (A\nabla u) + k_0^2 u = 0, \tag{1.3}$$

where the coefficient matrix

$$A(x) = \begin{bmatrix} \frac{1}{\varepsilon_{\perp}(x)} & 0 \\ 0 & \frac{1}{\varepsilon_{\parallel}(x)} \end{bmatrix}. \tag{1.4}$$

It is useful to note that $PA(x)$, rather than $A(x)$, is the inverse of the 2D permittivity tensor $\boldsymbol{\varepsilon}(x)$, in which P is the 2×2 permutation matrix corresponding to switching the rows. In a homogeneous medium, we set the permittivity values as $\varepsilon_{\perp}(x) \equiv \varepsilon_1$ and $\varepsilon_{\parallel}(x) \equiv \varepsilon_2$, where the complex-valued permittivities ε_1 and ε_2 satisfy

$$\mathrm{Re}\varepsilon_1 \cdot \mathrm{Re}\varepsilon_2 < 0 \quad \text{and} \quad \mathrm{Im}\varepsilon_j > 0 \quad (j = 1, 2).$$

Namely, the hyperbolic medium considered here is lossy.

Assume that a hyperbolic metamaterial with permittivity values $\varepsilon_{\perp}(x) \equiv \varepsilon_1^{(1)}$ and $\varepsilon_{\parallel}(x) \equiv \varepsilon_2^{(1)}$ occupies a bounded simply connected domain Ω_1. It is placed in an isotropic medium (e.g., vacuum, silicon) or is embedded in another hyperbolic metamaterial with the permittivity values $\varepsilon_{\perp}(x) \equiv \varepsilon_1^{(2)}$ and $\varepsilon_{\parallel}(x) \equiv \varepsilon_2^{(2)}$, which occupies the region $\Omega_2 = \mathbb{R}^2 \backslash \bar{\Omega}$. When a near-field source is excited in the interior or exterior domain, the magnetic field u satisfies

$$\nabla \cdot (A_j \nabla u_j) + k_0^2 u_j = f_j \quad \text{in } \Omega_j, \quad j = 1, 2, \tag{1.5}$$

in which

$$A_j = \begin{bmatrix} \left(\varepsilon_1^{(j)}\right)^{-1} & 0 \\ 0 & \left(\varepsilon_2^{(j)}\right)^{-1} \end{bmatrix}.$$

There holds $\varepsilon_1^{(2)} = \varepsilon_2^{(2)}$ when the exterior region is isotropic. The source f_j attains a compact support in Ω_j. Across the interface $\Gamma := \partial\Omega_1$, the continuity of the electric and magnetic fields leads to the condition

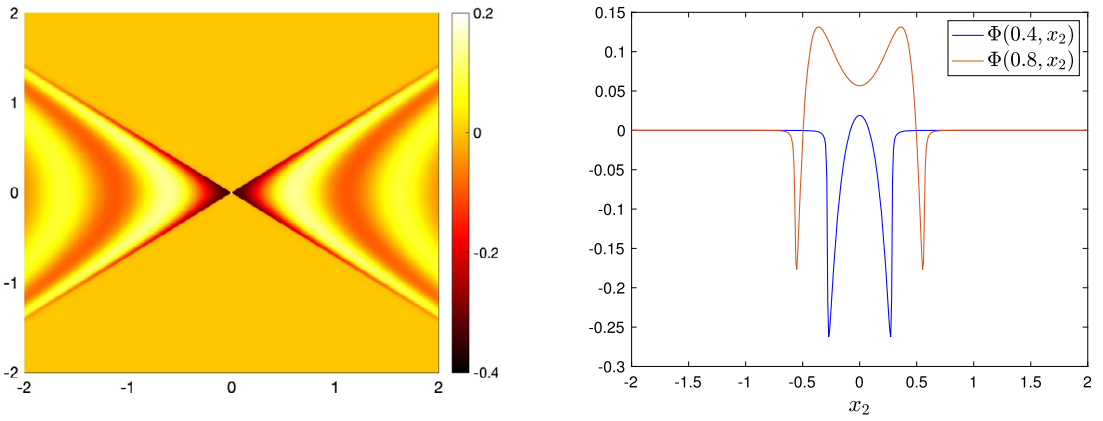

Fig. 1. Left: The real part of the fundamental solution $\Phi(x_1, x_2)$ in the hyperbolic medium with $\varepsilon_1 = 1 + 0.02i$ and $\varepsilon_2 = -2 + 0.02i$. The source is located at the origin, and the wavenumber $k_0 = 2\pi$. Right: cross-sectional plot of $\Phi(x_1, x_2)$ when $x_1 = 0.4$ and 0.8. $\Phi(x_1, x_2)$ attains sharp transitions near the boundary of the propagating cone $\mathcal{C}$. (For interpretation of the colors in the figure(s), the reader is referred to the web version of this article.)

$$u_1 = u_2, \quad A_1 \nabla u_1 \cdot \nu = A_2 \nabla u_2 \cdot \nu, \tag{1.6}$$

where ν represents the unit outward normal along the interface Γ. In addition to (1.5) and (1.6), the wave field u_2 in the exterior domain is outgoing when the exterior medium is isotropic. When the exterior medium is hyperbolic, u_2 is outgoing within the propagation cone with decreasing magnitude (due to the material loss) and it decays exponentially outside the propagating cone. In both configurations, u_2 satisfies the well-known Sommerfeld radiation condition [12]. This will be enforced automatically by using the Green's function and the integral equation formulation here.

Remark 1. One can formulate the scattering problem (1.5) in a bounded domain by using the Dirichlet-to-Neumann map along the domain boundary. Note that the hyperbolic medium is lossy with nonzero imaginary part for the permittivity values. Hence it can be shown from the Lax-Milgram theorem and the unique continuation principle that the corresponding boundary value problem is well-posed. However, the well-posedness of the boundary value problem for lossless hyperbolic medium is still open. Initial attempt has been reported in [3] for boundary value problems with special anisotropy directions and spherical geometry.

1.3. Computational challenges

Due to indefiniteness of the permittivity tensor, one important feature of a hyperbolic medium is the preferential wave propagation inside the cone

$$\mathcal{C} := \{x;\ \mathrm{Re}(x^T A^{-1} x) > 0\}.$$

The half cone angle is given by $\arctan\sqrt{-\frac{\mathrm{Re}\,\varepsilon_1}{\mathrm{Re}\,\varepsilon_2}}$ and $\arctan\sqrt{-\frac{\mathrm{Re}\,\varepsilon_2}{\mathrm{Re}\,\varepsilon_1}}$ when $\mathrm{Re}\,\varepsilon_1 > 0$ and $\mathrm{Re}\,\varepsilon_1 < 0$, respectively. Namely, the wave propagates within this cone but decays exponentially outside of the cone [21]. See, for instance, Fig. 1 for the fundamental solution of (1.3) and the numerical simulations for wave propagation in hyperbolic media presented in Section 4. In particular, when the source is located at the origin, one observes that the imaginary part of the argument z in the Hankel function $H_0^1(z)$ increases as the target point moves away from the cone boundary in $\mathbb{R}^2 \backslash \mathcal{C}$ and the fundamental solution decays exponentially accordingly. This induces sharp transition of the solution across the cone boundary when wave starts decaying/growing exponentially. The domain discretization methods such as finite element or finite difference are computationally very expensive to resolve such singular behaviors of the solution. Here we propose a boundary element method for solving for the transmission problem (1.5). Integral equation solvers have played an increasing role in the computational electromagnetics in the past several decades due to its powerfulness in solving large-scale problems by discretization over the boundaries of the objects only; see the monographs [1,10–12,27,32] and the references therein. The application of the integral equation method for the hyperbolic media requires us to address several new computational challenges as described below.

First, the fundamental solution in the hyperbolic medium is propagating inside the cone $\mathcal{C}$ and it decays exponentially across the cone boundary and outside. As a result, when computing the stiffness matrices in the boundary element method, one needs to apply adaptive numerical quadrature rules to evaluate the integrals with the fundamental solution or its derivatives as kernels in order to achieve sufficient accuracy for discretization. Second, the solution of the integral equation formulation along the interface Γ attains sharp transitions when wave front reaches the boundary, especially for hyperbolic media with small loss (see Section 4). Here we employ a two-level a posteriori error estimator and an adaptive mesh

refinement procedure to resolve the singularity of the integral equation solution in an accurate and efficient manner. The theory and computation for the adaptive boundary element methods (BEM) are mature in solving elliptic boundary value problems [20]. By using a posteriori error estimator, the adaptive procedure chooses a sequence of meshes such that the numerical error decays in an optimal manner with increasing dimension of the approximation spaces. There exist a variety of error estimators for elliptic boundary value problems, including residual type estimators, space enrichment type estimators, averaging estimators, etc [6–9,18,19,22,23,41]. The two-level a posteriori error estimator proposed here for the hyperbolic transmission problem belongs to the family of the space enrichment type estimators. The principal idea is to use improved approximation of solutions $u_{h/2}$ and $\partial_{\tilde{\nu}} u_{h/2}$ obtained over a uniform refined mesh with mesh size $h/2$ to replace the exact solution u and $\partial_{\tilde{\nu}} u$ in the numerical error $\|u-u_h\|$ and $\|\partial_{\tilde{\nu}} u - \partial_{\tilde{\nu}} u_h\|$. The Dörfler strategy is then applied to mark and refine the mesh where local errors $\|u_{h/2}-u_h\| + \|\partial_{\tilde{\nu}} u_{h/2} - \partial_{\tilde{\nu}} u_h\|$ are large. Such an adaptive procedure allows for the reduction of the number of the degrees of freedom significantly while achieving desired accuracy for the solution, as demonstrated by the numerical examples in Section 4. The goal of our work in this paper is to demonstrate the efficacy and accuracy of the adaptive algorithm for the two dimensional problems. Its application in three dimensions will be investigated in the forthcoming work.

The rest of the paper is organized as follows. In Section 2 we introduce layer potentials and derive their limits as the target points approach the boundary. The limiting formulas recover the formulas in the isotropic medium when $\varepsilon_1 = \varepsilon_2$. The boundary integral equation for the transmission problem (1.5) is then formulated in Section 2. The adaptive Galerkin boundary element method is described in Section 3, where we introduce the adaptive numerical quadrature and the two-level a posteriori error estimator. Several numerical examples are given in Section 4 to illustrate the accuracy and efficiency of the adaptive algorithm. The paper is concluded with brief remark about the proposed computational approach and the future work along this direction.

2. Layer potentials and boundary integral equations for the transmission problem

2.1. Layer potentials and integral operators

Here and henceforth, for a hyperbolic material with $\varepsilon_\perp(x) \equiv \varepsilon_1$ and $\varepsilon_\parallel(x) \equiv \varepsilon_2$, we let

$$\tilde{r}(x,y) = \sqrt{(x-y)^T A^{-1}(x-y)},$$

where the matrix A is given in (1.4) and the function $\sqrt{z}$ is understood as an analytic function defined in the domain $\mathbf{C}\backslash\{-it : t \geq 0\}$ such that $\sqrt{z} = |z|^{\frac{1}{2}} e^{\frac{1}{2} i \arg z}$. Note that when $\mathrm{Im}\varepsilon_j > 0$ $(j = 1, 2)$, $\tilde{r}(x,y)$ is complex-valued lying in the first quadrant of the complex plane. We emphasize that $\mathrm{Im}\varepsilon_j > 0$ is necessary to guarantee that $\tilde{r}(x,y) \neq 0$ when $x \neq y$ and the fundamental solution of (1.3) is well-defined for $x \neq y$. Let $\tilde{\nu} = A\nu$ be the A-deformed normal vector over the interface Γ. Correspondingly, the derivative of a given function φ along the direction $\tilde{\nu}$ is defined as

$$\frac{\partial \varphi}{\partial \tilde{\nu}} = \nabla\varphi \cdot \tilde{\nu} = \left[\frac{1}{\varepsilon_1}\frac{\partial \varphi}{\partial x_1}, \frac{1}{\varepsilon_2}\frac{\partial \varphi}{\partial x_2}\right] \cdot \nu.$$

Let $\Phi(x,y) = \dfrac{i}{4}\sqrt{\varepsilon_1\varepsilon_2} H_0^{(1)}\left(k_0 \tilde{r}(x,y)\right)$ be the fundamental solution which satisfies (1.3) when $x \neq y$. Here $H_0^{(1)}(r)$ represents the zero order Hankel function of the first kind. As $|x-y| \to \infty$, $\Phi(x,y)$ is outgoing within the propagation cone $\mathcal{C}$ and decays exponentially near and outside the cone. Ω is a bounded simply connected domain with the boundary Γ of class C^2. Given the density function φ over Γ, the single and double layer potentials are defined by

$$v(x) = \int_\Gamma \Phi(x,y)\varphi(y)\, ds_y \quad \text{and} \quad w(x) = \int_\Gamma \frac{\partial \Phi(x,y)}{\partial \tilde{\nu}(y)} \varphi(y)\, ds_y \quad \text{for} \quad x \notin \Gamma. \tag{2.1}$$

It is well-known that the single layer potential $v(x)$ is continuous throughout $\mathbb{R}^2$. In what follows, for completeness we derive the limits of the double layer potential and the derivatives of two layer potentials as x approaches Γ. Although the derivation follows the similar lines as the proof for the isotropic medium, the anisotropy requires special treatment for the new integrals and their decompositions, especially in Lemmas 2.1 and 2.3, and Proposition 2.4. Note also that the limiting formulas now depend on the anisotropy of the medium.

Lemma 2.1. *The double-layer potential $w(x)$ with the continuous density φ can be continuously extended from Ω to $\bar{\Omega}$ and $\mathbb{R}^2\backslash\bar{\Omega}$ to $\mathbb{R}^2\backslash\Omega$ respectively with the limit*

$$w_\pm(x) = \int_\Gamma \frac{\partial \Phi(x,y)}{\partial \tilde{\nu}(y)} \varphi(y)\, ds_y \pm \frac{1}{2}\varphi(x) \quad \textit{for } x \in \Gamma, \tag{2.2}$$

where

$$w_{\pm}(x) = \lim_{h>0,h\to 0} w(x \pm h\nu(x)).$$

Proof. Let $\Phi_0(x, y) = -\frac{1}{2\pi}\sqrt{\varepsilon_1\varepsilon_2}\ln(\tilde{r}(x, y))$ be the fundamental solution of (1.3) when $k_0 = 0$, and w_0 be the corresponding double layer potential:

$$w_0(x) = \int_\Gamma \frac{\partial \Phi_0(x, y)}{\partial \tilde{\nu}(y)}\varphi(y)\, ds_y.$$

Note that the difference of two double layer potentials $w(x)$ and $w_0(x)$ is continuous in $\mathbb{R}^2$, thus it suffices to verify (2.2) for $w_0(x)$. The proof can be further reduced to the special case when the density function $\varphi \equiv 1$, this is because for an arbitrary density function φ, one can write the double layer potential as

$$w_0(x) = \varphi(x)\int_\Gamma \frac{\partial \Phi_0(x, y)}{\partial \tilde{\nu}(y)}\, ds_y + \int_\Gamma \frac{\partial \Phi_0(x, y)}{\partial \tilde{\nu}(y)}(\varphi(y) - \varphi(x))\, ds_y,$$

and the latter is continuous throughout $\mathbb{R}^2$ when φ is continuous. Next we verify the assertion by assuming that $\varphi(x) \equiv 1$ and showing that

$$w_0(x) = \begin{cases} 0, & x \in \mathbb{R}^2\backslash\bar{\Omega}, \\ -\frac{1}{2}, & x \in \Gamma, \\ -1, & x \in \Omega. \end{cases} \tag{2.3}$$

When $x \in \mathbb{R}^2\backslash\bar{\Omega}$, noting that $\Phi_0(x, y)$ solves (1.3) with $k_0 = 0$ in Ω, it is obvious $w_0(x) = 0$ by applying the Green's formula. Now if $x \in \Gamma$, let $B_\delta(x)$ be the small disk with radius δ centered at x and $\partial B_\delta(x)$ be its boundary. It follows from the Green's formula that

$$\int_\Gamma \frac{\partial \Phi_0(x, y)}{\partial \tilde{\nu}(y)}\, ds_y = \lim_{\delta\to 0}\int_{\partial B_\delta(x)\cap\Omega} \frac{\partial \Phi_0(x, y)}{\partial \tilde{\nu}(y)}\, ds_y,$$

where ν denotes the unit normal exterior to $B_\delta(x)$. A direct calculation yields

$$\int_{\partial B_\delta(x)\cap\Omega} \frac{\partial \Phi_0(x, y)}{\partial \tilde{\nu}(y)}\, ds_y = -\frac{1}{2\pi}\sqrt{\varepsilon_1\varepsilon_2}\int_{\theta_1(\delta)}^{\theta_2(\delta)} \frac{r^2}{\tilde{r}^2}\, d\theta = -\frac{1}{2\pi}\int_{\theta_1(\delta)}^{\theta_2(\delta)} \frac{\sqrt{\varepsilon_1\varepsilon_2}}{\varepsilon_1\cos^2\theta + \varepsilon_2\sin^2\theta}\, d\theta \tag{2.4}$$

in the polar coordinate, where $r^2 = (x_1 - y_1)^2 + (x_2 - y_2)^2$ and $\tilde{r}^2 = \varepsilon_1(x_1 - y_1)^2 + \varepsilon_2(x_2 - y_2)^2$. Hence,

$$\int_\Gamma \frac{\partial \Phi_0(x, y)}{\partial \tilde{\nu}(y)}\, ds_y = \lim_{\delta\to 0} -\frac{1}{2\pi}\sqrt{\frac{\varepsilon_1}{\varepsilon_2}}\int_{\theta_1(\delta)}^{\theta_2(\delta)} \frac{\sec^2\theta}{\tan^2\theta + \varepsilon_1/\varepsilon_2}\, d\theta.$$

By evaluating the above integral explicitly and noting that $\lim_{\delta\to 0}(\theta_2(\delta) - \theta_1(\delta)) = \pi$, we obtain that $w_0(x) = -\frac{1}{2}$. A parallel calculation leads to $w_0(x) = -1$ for $x \in \Omega$, for which there holds $\theta_2(\delta) - \theta_1(\delta) = 2\pi$. □

Proposition 2.2. *The derivative of the single-layer potential $v(x)$ with the continuous density φ can be continuously extended from Ω to $\bar{\Omega}$ and $\mathbb{R}^2\backslash\bar{\Omega}$ to $\mathbb{R}^2\backslash\Omega$ respectively with the limit*

$$\frac{\partial v_{\pm}(x)}{\partial \tilde{\nu}} = \int_\Gamma \frac{\partial \Phi(x, y)}{\partial \tilde{\nu}(x)}\varphi(y)\, ds_y \mp \frac{1}{2}\varphi(x) \quad \text{for } x \in \Gamma, \tag{2.5}$$

where

$$\frac{\partial v_{\pm}(x)}{\partial \tilde{\nu}} = \lim_{h>0,h\to 0} \nabla v(x \pm h\nu(x)) \cdot \tilde{\nu}(x).$$

Proof. This can be observed from the formula

$$\nabla v(x \pm h\nu(x)) \cdot \tilde{\nu}(x) = -w(x \pm h\nu(x)) + \int_\Gamma \nabla_y \Phi(x \pm h\nu(x), y) \cdot (\tilde{\nu}(y) - \tilde{\nu}(x))\varphi(y)\, ds_y,$$

wherein we have used the relation $\nabla_x \Phi(x, y) = -\nabla_y \Phi(x, y)$. Note that the second term is continuous in $\mathbb{R}^2$, thus an application of Lemma 2.1 leads to (2.5). □

Lemma 2.3. *The gradient of the single layer potential $v(x)$ with the density $\varphi \in C^1(\Gamma)$ can be continuously extended from Ω to $\bar{\Omega}$ and $\mathbb{R}^2\backslash\bar{\Omega}$ to $\mathbb{R}^2\backslash\Omega$ respectively with the limit*

$$\nabla v_{\pm}(x) = \int_{\Gamma} \nabla_x \Phi(x, y)\varphi(y)\, ds_y \mp \frac{1}{2}\varphi(x)\, e_{\nu(x)} \quad \text{for } x \in \Gamma. \tag{2.6}$$

In the above, $\nabla v_{\pm}(x) = \lim_{h>0, h\to 0} \nabla v(x \pm h\nu(x))$, and the vector $e_{\nu(x)}$ is given by $e_{\nu(x)} = \dfrac{\nu(x)}{\nu(x)\cdot\tilde{\nu}(x)}$.

Proof. For $y \in \Gamma$, let $\nu(y) = [\nu_1(y), \nu_2(y)]^T$ and $\tau(y) = [-\nu_2(y), \nu_1(y)]^T$ be the normal and tangential vector respectively. For $x \neq y$, one can decompose $\nabla_y \Phi(x, y)$ as

$$\nabla_y \Phi(x, y) = \frac{\partial \Phi(x, y)}{\partial \tilde{\nu}(y)}\, e_{\nu(y)} + \frac{\partial \Phi(x, y)}{\partial \tau(y)}\, e_{\tau(y)}, \tag{2.7}$$

where

$$e_{\nu(y)} = \frac{1}{\nu(y)\cdot\tilde{\nu}(y)} \begin{bmatrix} \nu_1(y) \\ \nu_2(y) \end{bmatrix} \quad \text{and} \quad e_{\tau(y)} = \frac{1}{\nu(y)\cdot\tilde{\nu}(y)} \begin{bmatrix} -\nu_2(y)/\varepsilon_2 \\ \nu_1(y)/\varepsilon_1 \end{bmatrix}.$$

For fixed $z \in \Gamma$, set $x = z + h\nu(x)$ with $0 < h \ll 1$. Noting that $\nabla_x \Phi(x, y) = -\nabla_y \Phi(x, y)$ and in light of the decomposition (2.7), we have

$$\int_{\Gamma} \nabla_x \Phi(x, y)\varphi(y)\, ds_y = -\int_{\Gamma} \frac{\partial \Phi(x, y)}{\partial \tilde{\nu}(y)} \varphi(y) e_{\nu(y)}\, ds_y - \int_{\Gamma} \frac{\partial \Phi(x, y)}{\partial \tau(y)} \varphi(y) e_{\tau(y)}\, ds_y.$$

By letting $h \to 0$, the following relation holds:

$$\begin{aligned}
\lim_{h\to 0} \int_{\Gamma} \frac{\partial \Phi(x, y)}{\partial \tilde{\nu}(y)} \varphi(y) e_{\nu(y)}\, ds_y &= \int_{\Gamma} \frac{\partial \Phi(z, y)}{\partial \tilde{\nu}(y)} \varphi(y) e_{\nu(y)}\, ds_y + \frac{1}{2}\varphi(z)\cdot e_{\nu(z)}, \\
\lim_{h\to 0} \int_{\Gamma} \frac{\partial \Phi(x, y)}{\partial \tau(y)} \varphi(y) e_{\tau(y)}\, ds_y &= -\lim_{h\to 0} \int_{\Gamma} \Phi(x, y) \frac{d(\varphi(y) e_{\tau(y)})}{d\tau(y)}\, ds_y \\
&= -\int_{\Gamma} \Phi(z, y) \frac{d(\varphi(y) e_{\tau(y)})}{d\tau(y)}\, ds_y \\
&= \int_{\Gamma} \frac{\partial \Phi(z, y)}{\partial \tau(y)} \varphi(y) e_{\tau(y)}\, ds_y.
\end{aligned}$$

Therefore,

$$\begin{aligned}
\lim_{h\to 0} \int_{\Gamma} \nabla_x \Phi(x, y)\varphi(y)\, ds_y &= -\int_{\Gamma} \left(\frac{\partial \Phi(z, y)}{\partial \tilde{\nu}(y)} e_{\nu(y)} + \frac{\partial \Phi(z, y)}{\partial \tau(y)} e_{\tau(y)} \right) \varphi(y)\, ds_y - \frac{1}{2}\varphi(z)\cdot e_{\nu(z)} \\
&= \int_{\Gamma} \nabla_z \Phi(z, y)\varphi(y)\, ds_y - \frac{1}{2}\varphi(z)\cdot e_{\nu(z)},
\end{aligned}$$

where we use (2.7) and the relation $\nabla_z \Phi(z, y) = -\nabla_y \Phi(z, y)$ again. The proof for $x = z - h\nu(x)$ is parallel. □

Proposition 2.4. *Let $w(x)$ be the double layer potential defined in (2.1) and $\varphi \in C^1(\Gamma)$, then*

$$\frac{\partial w_{\pm}(x)}{\partial \tilde{\nu}} = \frac{1}{\varepsilon_1 \varepsilon_2} \frac{d}{ds_x} \int_{\Gamma} \Phi(x, y) \frac{d\varphi(y)}{ds}\, ds_y + k_0^2 \int_{\Gamma} \Phi(x, y)\varphi(y)(\nu(x)\cdot\tilde{\nu}(y))\, ds_y \quad \text{for } x \in \Gamma, \tag{2.8}$$

where $\dfrac{\partial w_{\pm}(x)}{\partial \tilde{\nu}} = \lim_{h>0, h\to 0} \nabla w(x \pm h\nu(x))\cdot\tilde{\nu}(x)$, and $\frac{d}{ds}$ denotes the derivative with respect to the arc length.

Proof. For $y \in \Gamma$, let $\tau(y)^{\perp} = [\tau_2(y), -\tau_1(y)]^T = \nu(y)$. If $x \notin \Gamma$, using the relation

$$\frac{\partial \Phi(x, y)}{\partial \tilde{\nu}(y)} = \nabla_y \Phi(x, y)\cdot\tilde{\nu}(y) = -\nabla_x \Phi(x, y)\cdot\tilde{\nu}(y) = -\left[\frac{1}{\varepsilon_1} \frac{\partial \Phi(x, y)}{\partial x_1},\ \frac{1}{\varepsilon_2} \frac{\partial \Phi(x, y)}{\partial x_2} \right] \cdot \tau(y)^{\perp},$$

we have

$$\nabla_x \frac{\partial \Phi(x,y)}{\partial \tilde{\nu}(y)} = -\nabla_x \left(\frac{\tau_2(y)}{\varepsilon_1} \frac{\partial \Phi(x,y)}{\partial x_1} - \frac{\tau_1(y)}{\varepsilon_2} \frac{\partial \Phi(x,y)}{\partial x_2} \right)$$
$$= \left[\frac{\tau_1(y)}{\varepsilon_2} \frac{\partial^2 \Phi(x,y)}{\partial x_1 \partial x_2} - \frac{\tau_2(y)}{\varepsilon_1} \frac{\partial^2 \Phi(x,y)}{\partial x_1^2}, \ \frac{\tau_1(y)}{\varepsilon_2} \frac{\partial^2 \Phi(x,y)}{\partial x_2^2} - \frac{\tau_2(y)}{\varepsilon_1} \frac{\partial^2 \Phi(x,y)}{\partial x_1 \partial x_2} \right]^T.$$

By using the equation (1.3) and the relation $\nabla_x \Phi(x,y) = -\nabla_y \Phi(x,y)$, it follows that

$$\nabla_x \frac{\partial \Phi(x,y)}{\partial \tilde{\nu}(y)} = \left[\frac{\tau_1(y)}{\varepsilon_2} \frac{\partial^2 \Phi(x,y)}{\partial x_1 \partial x_2} + \frac{\tau_2(y)}{\varepsilon_2} \frac{\partial^2 \Phi(x,y)}{\partial x_2^2}, \ -\frac{\tau_1(y)}{\varepsilon_1} \frac{\partial^2 \Phi(x,y)}{\partial x_1^2} - \frac{\tau_2(y)}{\varepsilon_1} \frac{\partial^2 \Phi(x,y)}{\partial x_1 \partial x_2} \right]^T$$
$$+ k_0^2 \Phi(x,y) \tau(y)^\perp$$
$$= \left[-\frac{1}{\varepsilon_2} \frac{\partial}{\partial x_2} \frac{\partial \Phi(x,y)}{\partial \tau_y}, \ \frac{1}{\varepsilon_1} \frac{\partial}{\partial x_1} \frac{\partial \Phi(x,y)}{\partial \tau_y} \right]^T + k_0^2 \Phi(x,y) \nu(y).$$

Hence, applying the integration by parts leads to

$$A \nabla_x \int_\Gamma \frac{\partial \Phi(x,y)}{\partial \tilde{\nu}(y)} \varphi(y) ds_y = \frac{1}{\varepsilon_1 \varepsilon_2} \left(\nabla_x \int_\Gamma \Phi(x,y) \frac{d\varphi(y)}{ds} ds_y \right)^\perp + k_0^2 \int_\Gamma \Phi(x,y) \varphi(y) \tilde{\nu}(y) ds_y. \tag{2.9}$$

Now for fixed $z \in \Gamma$, we set $x = z + h\nu(z)$. By virtue of (2.9) and Lemma 2.3, it follows that

$$\lim_{h\to 0} \nabla w(z + h\nu(z)) \cdot \tilde{\nu}(z)$$
$$= \lim_{h\to 0} \frac{1}{\varepsilon_1 \varepsilon_2} \left(\nabla \int_\Gamma \Phi(z + h\nu(z), y) \frac{d\varphi(y)}{ds} ds_y \right)^\perp \cdot \nu(z) + k_0^2 \int_\Gamma \Phi(z,y) \varphi(y) (\nu(z) \cdot \tilde{\nu}(y)) ds_y$$
$$= \frac{1}{\varepsilon_1 \varepsilon_2} \left(\nabla_z \int_\Gamma \Phi(z,y) \frac{d\varphi(y)}{ds} ds_y - \frac{1}{2} \varphi(z) e_{\nu(z)} \right)^\perp \cdot \nu(z) + k_0^2 \int_\Gamma \Phi(z,y) \varphi(y) (\nu(z) \cdot \tilde{\nu}(y)) ds_y.$$

A straightforward calculation leads to

$$\frac{\partial w_+(z)}{\partial \tilde{\nu}} = \frac{1}{\varepsilon_1 \varepsilon_2} \frac{d}{ds_z} \int_\Gamma \Phi(z,y) \frac{d\varphi(y)}{ds} ds_y + k_0^2 \int_\Gamma \Phi(z,y) \varphi(y) (\nu(z) \cdot \tilde{\nu}(y)) ds_y.$$

Similarly, by setting $x = z - h\nu(z)$, one can obtain the same formula for $\frac{\partial w_-(z)}{\partial \tilde{\nu}}$. □

2.2. Boundary integral equation formulation for the transmission problem

Let $\Phi_j(x,y) = \frac{i}{4} \sqrt{\varepsilon_1^{(j)} \varepsilon_2^{(j)}} H_0^{(1)} \left(k \tilde{r}_j(x,y) \right)$ be the fundamental solution in the domain Ω_j, where $\tilde{r}_j = (x-y)^T A_j^{-1} (x-y)$. Let $\tilde{\nu}_j = A_j \nu$ be the A_j-deformed normal vector over the interface Γ. We define the integral operators S_j, K_j, K_j' and N_j for $x \in \Gamma$ as follows:

$$[S_j \varphi](x) = \int_\Gamma \Phi_j(x,y) \varphi(y) ds_y, \tag{2.10}$$

$$[K_j \varphi](x) = \int_\Gamma \frac{\partial \Phi_j(x,y)}{\partial \tilde{\nu}_j(y)} \varphi(y) ds_y, \tag{2.11}$$

$$[K_j' \varphi](x) = \int_\Gamma \frac{\partial \Phi_j(x,y)}{\partial \tilde{\nu}_j(x)} \varphi(y) ds_y, \tag{2.12}$$

$$[N_j \varphi](x) = \frac{1}{\varepsilon_1^{(j)} \varepsilon_2^{(j)}} \frac{d}{ds_x} S_j \left(\frac{d\varphi}{ds} \right) + k_0^2 \nu(x) \cdot S_j(\varphi \tilde{\nu}_j) \tag{2.13}$$
$$= \frac{1}{\varepsilon_1^{(j)} \varepsilon_2^{(j)}} \frac{d}{ds_x} \int_\Gamma \Phi_j(x,y) \frac{d\varphi(y)}{ds} ds_y + k_0^2 \int_\Gamma \Phi_j(x,y) \varphi(y) (\nu(x) \cdot \tilde{\nu}_j(y)) ds_y.$$

Note that $\Phi_j(x,y)$ in the lossy hyperbolic medium attains the same singularity as the fundamental solution with $\varepsilon_1=\varepsilon_2=1$, thus from the standard theory of the boundary integral operators (cf. [30]), we have the following lemma for the above integral operators.

Lemma 2.5. *The operators $S_j: H^{-1/2}(\Gamma)\to H^{1/2}(\Gamma)$, $K_j: H^{1/2}(\Gamma)\to H^{1/2}(\Gamma)$, $K_j': H^{-1/2}(\Gamma)\to H^{-1/2}(\Gamma)$, and $N_j: H^{1/2}(\Gamma)\to H^{-1/2}(\Gamma)$ are bounded.*

Let

$$S=S_1-S_2,\quad K=K_1-K_2,\quad K'=K_1'-K_2',\quad N=N_1'-N_2'$$

be the difference of two integral operators with associated kernels. The volume integral operators P_j and Q_j are defined as

$$[P_j\varphi](x)=\int_{\Omega_j}\Phi_j(x,y)\varphi(y)\,dy,\quad \text{for } x\in\Gamma,$$
$$[Q_j\varphi](x)=\int_{\Omega_j}\frac{\partial\Phi_j(x,y)}{\partial\nu(x)}\varphi(y)\,dy,\quad \text{for } x\in\Gamma.$$

Applying the Green's formula in Ω_1 and using the formula (2.3), we obtain for $x\in\Omega_1$ that

$$u_1(x)=\int_\Gamma \Phi_1(x,y)\frac{\partial u_1(y)}{\partial\tilde\nu_1(y)}-\frac{\partial\Phi_1(x,y)}{\partial\tilde\nu_1(y)}u_1(y)\,ds_y-\int_{\Omega_1}\Phi_1(x,y)f_1(y)\,dy. \tag{2.14}$$

Similarly, for $x\in\Omega_2$ there holds

$$u_2(x)=\int_\Gamma \frac{\partial\Phi_2(x,y)}{\partial\tilde\nu_2(y)}u_2(y)-\Phi_2(x,y)\frac{\partial u_2(y)}{\partial\tilde\nu_2(y)}\,ds_y-\int_{\Omega_2}\Phi_2(x,y)f_2(y)\,dy. \tag{2.15}$$

Recall that $f_1(x)$ and $f_2(x)$ are localized sources with compact support, the volume integrals above only need to be evaluated over their support regions. By taking the limit of (2.14) and (2.15) when x approaches the interface Γ and applying Lemma 2.1, we achieve the integral equations on Γ:

$$\frac{1}{2}u_1=S_1\left(\frac{\partial u_1}{\partial\tilde\nu_1}\right)-K_1u_1-P_1f_1; \tag{2.16}$$
$$\frac{1}{2}u_2=K_2u_2-S_2\left(\frac{\partial u_2}{\partial\tilde\nu_2}\right)-P_2f_2. \tag{2.17}$$

For $x\in\Gamma$, evaluating $\nabla u_j(x\pm h\nu(x))\cdot\tilde\nu(x)$ in (2.14) and (2.15) respectively, and taking the limit when $h\to 0$ yields

$$\frac{1}{2}\frac{\partial u_1}{\partial\tilde\nu}=K_1'\left(\frac{\partial u_1}{\partial\tilde\nu_1}\right)-N_1u_1-Q_1f_1; \tag{2.18}$$
$$\frac{1}{2}\frac{\partial u_2}{\partial\tilde\nu}=N_2u_2-K_2'\left(\frac{\partial u_2}{\partial\tilde\nu_2}\right)-Q_2f_2, \tag{2.19}$$

where we have used Lemma 2.3 and Proposition 2.4.

By taking the sum (2.16) + (2.17) and (2.18) + (2.19) respectively, and applying the continuity condition (1.6) for the wave field across the interface, we obtain the following system of integral equations:

$$\begin{bmatrix} N & I-K' \\ I+K & -S\end{bmatrix}\begin{bmatrix}\phi^{(1)}\\ \phi^{(2)}\end{bmatrix}=\begin{bmatrix} g^{(1)}\\ g^{(2)}\end{bmatrix}. \tag{2.20}$$

In the above, $\phi^{(1)}=u_1=u_2$, $\phi^{(2)}=\frac{\partial u_1}{\partial\tilde\nu_1}=\frac{\partial u_2}{\partial\tilde\nu_2}$, and

$$g^{(1)}=-(Q_1f_1+Q_2f_2),\quad g^{(2)}=-(P_1f_1+P_2f_2).$$

We point out that integral equations in the form of (2.20) have been widely used in studies of acoustic, electromagnetic, and elastic transmission problems with isotropic media; see, for instance, [4,14,15,29] and the references therein.

For brevity of notation, we let

$$\mathbf{T}=\begin{bmatrix} N & I-K' \\ I+K & -S\end{bmatrix},\quad \boldsymbol{\phi}=\begin{bmatrix}\phi^{(1)}\\ \phi^{(2)}\end{bmatrix},\quad \boldsymbol{g}=\begin{bmatrix} g^{(1)}\\ g^{(2)}\end{bmatrix}. \tag{2.21}$$

In view of Lemma 2.5, the operator $\mathbf{T}$ is bounded from $H^{1/2}(\Gamma)\times H^{-1/2}(\Gamma)\to H^{-1/2}(\Gamma)\times H^{1/2}(\Gamma)$. Let $\mathcal{H}=H^{1/2}(\Gamma)\times H^{-1/2}(\Gamma)$ be the Hilbert space equipped with the inner product

$$\langle \boldsymbol{\phi},\boldsymbol{\psi}\rangle=\int_\Gamma \phi^{(1)}\bar{\psi}^{(1)}+\phi^{(2)}\bar{\psi}^{(2)}\,ds,$$

and $\mathcal{H}'=H^{-1/2}(\Gamma)\times H^{1/2}(\Gamma)$ be the dual space of $\mathcal{H}$. Then the weak formulation for the integral equation (2.20) reads as finding $\boldsymbol{\phi}\in\mathcal{H}$ such that

$$a(\boldsymbol{\phi},\boldsymbol{\psi})=\langle \boldsymbol{g},\boldsymbol{\psi}\rangle\quad\forall\boldsymbol{\psi}\in\mathcal{H}, \tag{2.22}$$

in which the sesquilinear form

$$a(\boldsymbol{\phi},\boldsymbol{\psi})=\langle \mathbf{T}\boldsymbol{\phi},\boldsymbol{\psi}\rangle=\langle N\phi^{(1)},\psi^{(1)}\rangle+\langle (I-K')\phi^{(2)},\psi^{(1)}\rangle+\langle (I+K)\phi^{(1)},\psi^{(2)}\rangle-\langle S\phi^{(2)},\psi^{(2)}\rangle.$$

Remark 2. One can show the well-posedness of the above formulation following the lines in [14,15]. As pointed out in Remark 1, the well-posedness holds for lossy hyperbolic media, for which the Lax-Milgram theorem can still be applied. However, one may lose the well-posedness if the hyperbolic medium becomes lossless.

3. Adaptive Galerkin boundary element method

3.1. Galerkin boundary element method

Let $\Gamma_h=\{E_1,E_2,\cdots,E_M\}$ be a mesh assigned on the interface Γ with the mesh size $h=\max_{1\le m\le M}|E_m|$, and $\mathcal{H}_h:=\mathcal{U}_h\times\mathcal{V}_h$ be the corresponding finite-dimensional space defined over Γ_h. Here $\mathcal{U}_h$ and $\mathcal{V}_h$ are the finite-dimensional approximation of the space $H^{1/2}(\Gamma)$ and $H^{-1/2}(\Gamma)$ respectively. The Galerkin boundary element method is to find $\boldsymbol{\phi}_h\in\mathcal{H}_h$ such that

$$a(\boldsymbol{\phi}_h,\boldsymbol{\psi}_h)=\langle \boldsymbol{g},\boldsymbol{\psi}_h\rangle\quad\forall\boldsymbol{\psi}_h\in\mathcal{H}_h. \tag{3.1}$$

Let $\left\{\phi_m^{(1)}\right\}_{m=1}^{M_1}$ and $\left\{\phi_m^{(2)}\right\}_{m=1}^{M_2}$ be the basis of the space $\mathcal{U}_h$ and $\mathcal{V}_h$ respectively. By representing the solution as $\phi_h^{(1)}(x)=\sum_{m=1}^{M_1}c_m^{(1)}\phi_m^{(1)}(x)$ and $\phi_h^{(2)}(x)=\sum_{m=1}^{M_2}c_m^{(2)}\phi_m^{(2)}(x)$, the Galerkin approximation (3.1) leads to the following linear system:

$$\begin{bmatrix} N_h & I_h'-K_h' \\ I_h+K_h & -S_h\end{bmatrix}\begin{bmatrix}\mathbf{c}^{(1)}\\ \mathbf{c}^{(2)}\end{bmatrix}=\begin{bmatrix} g_h^{(1)}\\ g_h^{(2)}\end{bmatrix}. \tag{3.2}$$

In the above, $\mathbf{c}^{(1)}$ and $\mathbf{c}^{(2)}$ represent the unknown vectors that take the following form:

$$\mathbf{c}^{(1)}=\left[c_1^{(1)},c_2^{(1)},\cdots,c_{M_1}^{(1)}\right],\quad \mathbf{c}^{(2)}=\left[c_1^{(2)},c_2^{(2)},\cdots,c_{M_2}^{(2)}\right].$$

The (m,n)-th entry of the matrices N_h, K_h, S_h, and I_h are given by

$$N_h(m,n)=\left\langle N\phi_n^{(1)},\phi_m^{(1)}\right\rangle,\quad K_h(m,n)=\left\langle K\phi_n^{(1)},\phi_m^{(2)}\right\rangle, \tag{3.3}$$

$$S_h(m,n)=\left\langle S\phi_n^{(2)},\phi_m^{(2)}\right\rangle,\quad I_h(m,n)=\left\langle \phi_n^{(1)},\phi_m^{(2)}\right\rangle. \tag{3.4}$$

I_h' and K_h' are the transposes of I_h and K_h respectively. In light of (2.13), we evaluate $N_h(m,n)$ using the formula

$$\left\langle N_j\phi_n^{(1)},\phi_m^{(1)}\right\rangle=-\frac{1}{\varepsilon_1^{(j)}\varepsilon_2^{(j)}}\left\langle S_j\frac{d\phi_n^{(1)}}{ds},\frac{d\phi_m^{(1)}}{ds}\right\rangle+k_0^2\left\langle S_j(\phi_n^{(1)}\tilde{\nu}_j)\cdot\nu,\phi_m^{(1)}\right\rangle,\quad j=1,2. \tag{3.5}$$

The m-th element for the vectors $g_h^{(1)}$ and $g_h^{(2)}$ are given by

$$g_h^{(1)}(m)=\left\langle g^{(1)},\phi_m^{(1)}\right\rangle,\quad g_h^{(2)}(m)=\left\langle g^{(2)},\phi_m^{(2)}\right\rangle.$$

3.2. Adaptive numerical integration

The entries of the local stiffness matrices (3.3) - (3.5) boil down to the evaluation of integral in the form of

$$e_{mn} = \int_{E_m}\int_{E_n} \Theta(x, y)\phi_n(y)\,\phi_m(x)\,ds_y ds_x,$$

in which $\Theta(x, y)$ represents the kernel $\Phi_j(x, y)$ or $\dfrac{\partial \Phi_j(x, y)}{\partial \tilde{y}_j(y)}$, and $\phi_m(x)$ represents the basis functions in $\mathcal{U}_h$ or $\mathcal{V}_h$. As pointed out in Section 1.3, the fundamental solution in the hyperbolic medium is propagating in the cone $\mathcal{C} = \{x;\, \mathrm{Re}(x^T A^{-1}x) > 0\}$ only, and it attains sharp transition near the cone boundary $\partial\mathcal{C}$. To capture the variation of the kernels accurately, we employ the adaptive numerical quadrature to compute e_{mn}. In more detail, for a given small real number $\tau > 0$, let us introduce the domain

$$\Omega_\tau = \{x;\, dist(x, \partial\mathcal{C}) < \tau\} \tag{3.6}$$

that includes the cone boundary. τ is chosen so that Ω_τ contains the region where $\Theta(x, y)$ attains very large derivatives. Let $E_{mn} = \{x - y\,;\, x \in E_m, y \in E_n\}$ be the set of relative locations between the source and target points when evaluating e_{mn}. If $E_{mn} \cap \Omega_\tau = \emptyset$, then $\Theta(x, y)$ changes smoothly over the domain $(x, y) \in E_m \times E_n$, thus there is no need for adaptivity and one can still apply fast algorithms, such as the fast multipole method, to evaluate e_{mn} for fixed m and all n satisfying $E_{mn} \cap \Omega_\tau = \emptyset$ in an efficient manner [10,25]. Otherwise, if $E_{mn} \cap \Omega_\tau \neq \emptyset$, we compute e_{mn} adaptively to resolve the kernels accurately as described below.

Note that when $m = n$, the kernel $\Theta(x, y)$ is weakly singular and the singular part of e_{mn} can be evaluated analytically. Hence we only need to consider the case when $m \neq n$ and $\Theta(x, y)$ is nonsingular. By a change of variable, e_{mn} is expressed as

$$e_{mn} = \int_{-1}^{1}\int_{-1}^{1} \Theta\big(x(t), y(s)\big)\phi_n\big(y(s)\big)\phi_m\big(x(t)\big)\,dsdt \tag{3.7}$$

in the parameter space. The integral in (3.7) is computed via the adaptive Lobatto quadrature rule [24]. Let $\left\{R_j^{(\ell)}\right\}_{j=1}^{J}$ be a decomposition of the whole integral region at level ℓ with small rectangles $R_j^{(\ell)}$. Starting from $\ell = 0$ and $J = 1$ with $R_1^{(0)} = [-1, 1] \times [-1, 1]$, the adaptive algorithm computes the integral recursively over the region $R_j^{(\ell)}$ by first dividing $R_j^{(\ell)}$ in half along t and s coordinate axis respectively to produce four new subregions $R_{j_1}^{(\ell+1)}$, $R_{j_2}^{(\ell+1)}$, $R_{j_3}^{(\ell+1)}$ and $R_{j_4}^{(\ell+1)}$, and then calculating the integral using the Lobatto quadrature rule over these four subregion regions. The recursive procedure stops when the relative difference of the two approximations at level ℓ and $\ell + 1$ is smaller than the prescribed tolerance. We refer the readers to [2] for more details of the recursive procedure. Since the region Ω_τ is usually thin with small τ ($\tau = 0.1$ is chosen in variety of numerical experiments demonstrated in Section 4), the cardinal number of the set $\{(m, n)|E_{mn} \cap \Omega_\tau \neq \emptyset\} \ll M^2$. In addition, the recursive adaptive Lobatto quadrature rule for the integral inside Ω_τ convergences fast, thus the adaptive integration only accounts for a small percentage of the overall cost in assembling the stiffness matrices.

3.3. The two-level a posteriori error estimator and mesh refinement

Let $\Gamma_h = \{E_1, E_2, \cdots, E_M\}$ be a mesh over Γ with the mesh size h, and $\hat{\Gamma}_h = \{\hat{E}_1, \hat{E}_2, \cdots, \hat{E}_{2M}\}$ be a uniform refinement of Γ_h with the mesh size $h/2$. The corresponding Galerkin solution in the finite-dimensional space $\mathcal{H}_h = \mathcal{U}_h \times \mathcal{V}_h$ and $\hat{\mathcal{H}}_h = \hat{\mathcal{U}}_h \times \hat{\mathcal{V}}_h$ is denoted as $\boldsymbol{\phi}_h$ and $\hat{\boldsymbol{\phi}}_h$, respectively. We use a two-level a posteriori error estimator where the exact solution in the numerical error $\|\hat{\boldsymbol{\phi}}_h - \boldsymbol{\phi}\|$ is replaced by the solution $\hat{\boldsymbol{\phi}}_h$ obtained over the uniformly refined mesh $\hat{\Gamma}_h$. This leads to the first $h - h/2$ based estimators

$$\eta^{(1)} = \|\hat{\phi}_h^{(1)} - \phi_h^{(1)}\|_{H^{1/2}(\Gamma)} \quad \text{and} \quad \eta^{(2)} = \|\hat{\phi}_h^{(2)} - \phi_h^{(2)}\|_{H^{-1/2}(\Gamma)}, \tag{3.8}$$

wherein $\boldsymbol{\phi}_h = [\phi_h^{(1)}, \phi_h^{(2)}]$ and $\hat{\boldsymbol{\phi}}_h = [\hat{\phi}_h^{(1)}, \hat{\phi}_h^{(2)}]$.

The estimators $\eta^{(1)}$ and $\eta^{(2)}$ defined above are simple, but they suffer certain practical computational constraints. First, the estimators $\eta^{(1)}$ and $\eta^{(2)}$ require the computation of the solutions $\boldsymbol{\phi}_h$ and $\hat{\boldsymbol{\phi}}_h$ at both discretization levels, which could be computationally burdensome. Note that $\hat{\boldsymbol{\phi}}_h$ is expected to be more accurate than $\boldsymbol{\phi}_h$, thus the latter becomes a temporary result that is not useful once $\eta^{(1)}$ and $\eta^{(2)}$ are calculated. In order to reduce the computational cost and avoid such redundancy, after $\hat{\boldsymbol{\phi}}_h$ is computed, following [20] we use $\hat{\boldsymbol{\phi}}_h$ to approximate the solution $\boldsymbol{\phi}_h$ by projecting the refined solution $\hat{\boldsymbol{\phi}}_h$ over the finite-dimensional space $\mathcal{H}_h$. In addition, we localize the estimators by using $h^{1/2}$-weighted H^1-seminorm for $\phi_h^{(1)}$

and L^2-norm for $\phi_h^{(2)}$, respectively. The localization yields error indicator over each element that is computable and can be used to design the mesh refinement strategy. More precisely, we define the second error estimators $\tilde{\eta}^{(1)}$ and $\tilde{\eta}^{(2)}$ as follows:

$$\tilde{\eta}^{(1)} = \left(\sum_{m=1}^{M} \rho^{(1)}(E_m) \right)^{1/2} \quad \text{and} \quad \tilde{\eta}^{(2)} = \left(\sum_{m=1}^{M} \rho^{(2)}(E_m) \right)^{1/2},$$

where the error indicators over each element E_m are given by

$$\rho_m^{(1)}(E_m) = |E_m| \cdot \left\| \frac{d}{ds} \left(\hat{\phi}_h^{(1)} - \Pi_h^{(1)} \hat{\phi}_h^{(1)} \right) \right\|^2_{L^2(E_m)} \quad \text{and} \quad \rho_m^{(2)}(E_m) = |E_m| \cdot \left\| \hat{\phi}_h^{(2)} - \Pi_h^{(2)} \hat{\phi}_h^{(2)} \right\|^2_{L^2(E_m)}, \tag{3.9}$$

and $\Pi_h^{(1)}$ $\left(\Pi_h^{(2)}\right)$ denotes the L^2-projection operator from $\hat{\mathcal{U}}_h$ to $\mathcal{U}_h$ ($\hat{\mathcal{V}}_h$ to $\mathcal{V}_h$). The total error estimator $\tilde{\eta}$ for $\boldsymbol{\phi}_h$ is defined as

$$\tilde{\eta} = \left(\sum_{m=1}^{M} \rho^{(1)}(E_m) + \rho^{(2)}(E_m) \right)^{1/2}. \tag{3.10}$$

Recall that $\hat{\phi}_h^{(1)}$ and $\hat{\phi}_h^{(2)}$ are the Galerkin approximations of the solution for the transmission problem and its normal derivative, we see that $\tilde{\eta}$ provides a $h^{1/2}$-weighted H^1-seminorm estimator for the solution u over the interface Γ. We point out that $\tilde{\eta}^{(j)}$ $(j = 1, 2)$ alone has been used as a posteriori error estimator for solving elliptic boundary value problems with Dirichlet or Neumann boundary conditions, and it has been shown that the estimator is efficient and reliable in the sense that the true error for the numerical solution is bounded below and above by the estimator $\tilde{\eta}^{(j)}$ [20]. Here we combine the two together in (3.10) as the error estimator for the transmission problem in the hyperbolic media. A variety of numerical examples in Section 4 demonstrate the effectiveness of the proposed error estimator. The theoretical investigation on its robustness remains to be studied in the future.

The Dörfler strategy is employed to mark and refine the mesh Γ_h using the error estimator $\tilde{\eta}$. For given $0 < \gamma < 1$, we find the minimal set $\mathcal{E} \subset \Gamma_h$ such that

$$\gamma \, \tilde{\eta}^2 \le \sum_{E \in \mathcal{E}} (\rho^{(1)}(E) + \rho^{(2)}(E)), \tag{3.11}$$

and each marked element in $\mathcal{E}$ is then divided into two sub-elements with equal size. The complete adaptive strategy starts from an initial discretization of the interface Γ. The calculation of the estimator (3.10) and the refinement procedure (3.11) is repeated until $\tilde{\eta} < \sigma$ for certain prescribed tolerance σ. This is summarized in the following algorithm:

Algorithm The adaptive boundary element method.

Given tolerance σ and the initial mesh size h, generate the initial $\Gamma_h^{(0)}$;
for $\ell = 0, 1, 2, \ldots, L$ **do**
  Let $\hat{\Gamma}_h^{(\ell)}$ be a uniform refinement of $\Gamma_h^{(\ell)}$;
  Apply the adaptive numerical integration over $\hat{\Gamma}_h^{(\ell)}$ to assemble the matrix in (3.2);
  Compute $\hat{\boldsymbol{\phi}}_h^{(\ell)}$ via (3.2) and compute the estimator $\tilde{\eta}$ by (3.9) and (3.10);
  if $\tilde{\eta} \ge \sigma$ **then**
    Choose the minimal subset $\mathcal{E} \subset \Gamma_h^{(\ell)}$ such that (3.11) is satisfied;
    Divide each element in $\mathcal{E}$ into two sub-elements to obtain $\Gamma_h^{(\ell+1)}$;
  else
    Stop and return the solution $\hat{\boldsymbol{\phi}}_h^{(\ell)}$;
  end if
end for

4. Numerical examples

We test the accuracy and efficiency of the adaptive boundary element method (BEM) in this section. Without loss of generality, we consider the point source functions in (1.5) when either f_1 or f_2 is a Dirac delta function. Throughout all the examples, τ is set as 0.1 in (3.6) for the domain Ω_τ used in the adaptive numerical integration. Recall that $\phi^{(1)} = u_1 = u_2$, $\phi^{(2)} = \frac{\partial u_1}{\partial \nu_1} = \frac{\partial u_2}{\partial \nu_2}$ are the Dirichlet and Neumann data over the interface Γ, which are approximated by the first-order linear element and the zero-order constant element respectively in the boundary element calculations. The corresponding numerical solutions returned from the adaptive algorithm are denoted by $\hat{\phi}_h^{(1)}$ and $\hat{\phi}_h^{(2)}$, which are obtained over the refined mesh $\hat{\Gamma}_h^{(\ell)}$. We also define the relative errors by letting

Table 1
The maximum and minimum mesh sizes $h_{\max}$ and $h_{\min}$ for $\Gamma_h^{(\ell)}$, and the relative errors $\hat{e}^{(1)}$ and $\hat{e}^{(2)}$ for the adaptive BEM and non-adaptive BEM (Example 1).

	Adaptive BEM					Non-adaptive BEM
DOF	$M^{(0)}=100$	$M^{(1)}=125$	$M^{(2)}=158$	$M^{(3)}=202$	$M^{(4)}=253$	$\bar{M}=700$
$h_{\max}$	0.1256	0.1256	0.1245	0.1245	0.1234	0.018
$h_{\min}$	0.0629	0.0349	0.0174	0.0087	0.0069	0.009
$\hat{e}^{(1)}$	0.0359	0.0145	0.0057	0.0047	0.0044	5.28×10^{-4}
$\hat{e}^{(2)}$	0.5685	0.3804	0.2965	0.1070	0.0745	0.0757

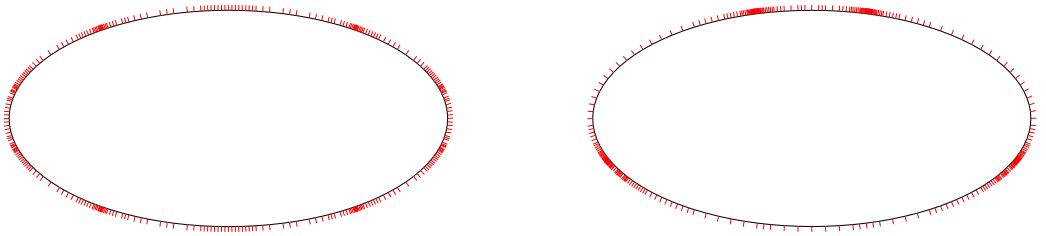

Fig. 2. The mesh $\Gamma_h^{(4)}$ over the boundary of the ellipse for Example 1 (left) and Example 2 (right).

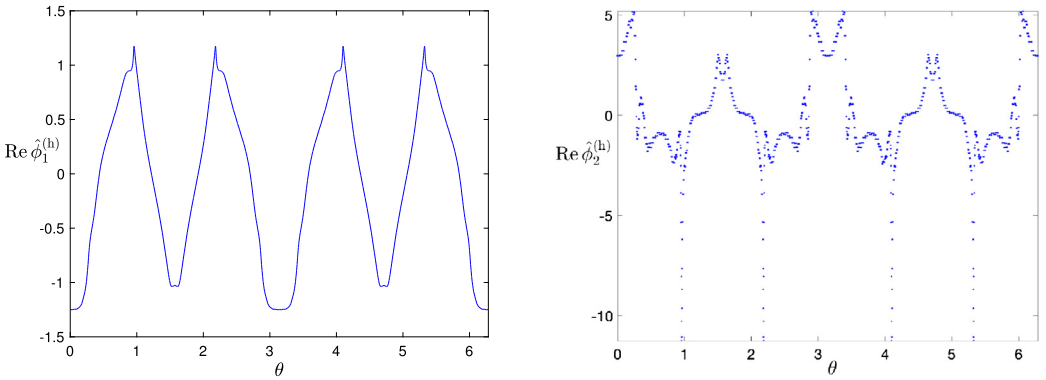

Fig. 3. The real parts of $\hat{\phi}_h^{(1)}$ and $\hat{\phi}_h^{(2)}$ obtained from the adaptive algorithm in Example 1. θ represents the polar angle over the ellipse.

$$\hat{e}^{(1)}=\frac{\|\phi^{(1)}-\hat{\phi}_h^{(1)}\|_{L^2(\Gamma)}}{\|\phi^{(1)}\|_{L^2(\Gamma)}} \quad \text{and} \quad \hat{e}^{(2)}=\frac{\|\phi^{(2)}-\hat{\phi}_h^{(2)}\|_{L^2(\Gamma)}}{\|\phi^{(2)}\|_{L^2(\Gamma)}},$$

in which $\phi^{(1)}$ and $\phi^{(2)}$ are reference solutions obtained with high-order accuracy.

Example 1. Assume that the interface Γ is an ellipse with semi-axes $a=2$ and $b=1$ respectively. The interior domain is a hyperbolic medium while the exterior domain is vacuum. The permittivity values in Ω_1 and Ω_2 are given by $\varepsilon_1^{(1)}=1+0.02i$, $\varepsilon_2^{(1)}=-2+0.02i$ and $\varepsilon_1^{(2)}=\varepsilon_2^{(2)}=1$, respectively. The wavenumber $k_0=1$, and the source is located in Ω_1 such that $f_1=-\delta(x)$ and $f_2=0$. Due to the smoothness of the interface, we compute the reference solutions $\phi^{(1)}$ and $\phi^{(2)}$ with high-order accuracy by the Nyström scheme, which is a spectral method using the trigonometric interpolant over Γ [30]. By parameterizing the interface Γ with $x_1=a\cos\theta$ and $x_2=b\sin\theta$, the initial mesh $\Gamma_h^{(0)}$ is generated with grid points $\{(a\cos\theta_m, b\sin\theta_m)\}_{m=1}^{M^{(0)}}$, in which $\theta_m=\frac{2(m-1)\pi}{M^{(0)}}$.

Table 1 shows the mesh sizes and the corresponding numerical errors for different levels of refinements when the adaptive procedure is applied, in which $M^{(\ell)}$ denotes the number of grid points being used in the mesh $\Gamma_h^{(\ell)}$. As expected, the numerical error $\hat{e}^{(1)}$ for the Dirichlet data $\phi^{(1)}$ is relatively small over the initial mesh $\Gamma_h^{(0)}$, while $\hat{e}^{(2)}$ for the Neumann data is large due to the singular behavior of $\phi^{(2)}$. It is observed that the two-level a posteriori error estimator $\tilde{\eta}$ is effective in identifying the solution singularities and a local mesh refinement near the singularities reduces the numerical error significantly after each refinement. The adaptive procedure terminates with $\ell=4$ and the number of grid points is $M^{(4)}=253$ for the mesh $\Gamma_h^{(4)}$; see Fig. 2 (left) for a plot of the mesh $\Gamma_h^{(4)}$. The numerical solutions $\hat{\phi}_h^{(1)}$ and $\hat{\phi}_h^{(2)}$ in the final stage of the adaptive procedure are plotted in Fig. 3, which are solved over the mesh $\hat{\Gamma}_h^{(4)}$. The corresponding numerical

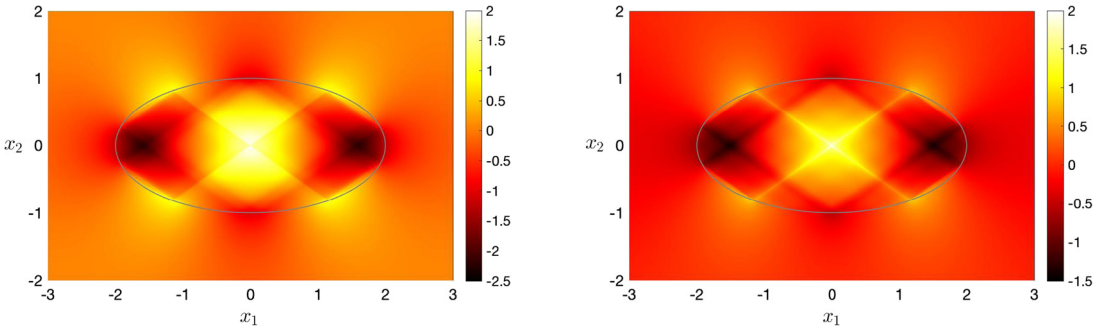

Fig. 4. Real (left) and imaginary part (right) of the wave field inside and outside the elliptical domain in Example 1.

Table 2
The maximum and minimum mesh sizes $h_{\max}$ and $h_{\min}$ for $\Gamma_h^{(\ell)}$, and the relative errors $\hat{e}^{(1)}$ and $\hat{e}^{(2)}$ for the adaptive BEM and non-adaptive BEM (Example 2).

	Adaptive BEM					Non-adaptive BEM
DOF	$M^{(0)}=100$	$M^{(1)}=125$	$M^{(2)}=157$	$M^{(3)}=199$	$M^{(4)}=249$	$\bar{M}=1000$
$h_{\max}$	0.1256	0.1256	0.1256	0.1256	0.1256	0.0126
$h_{\min}$	0.0629	0.0364	0.0182	0.0092	0.0046	0.0063
$\hat{e}^{(1)}$	0.0576	0.0154	0.0042	0.0034	0.0034	2.16×10^{-4}
$\hat{e}^{(2)}$	0.6957	0.4197	0.1881	0.0928	0.0616	0.0639

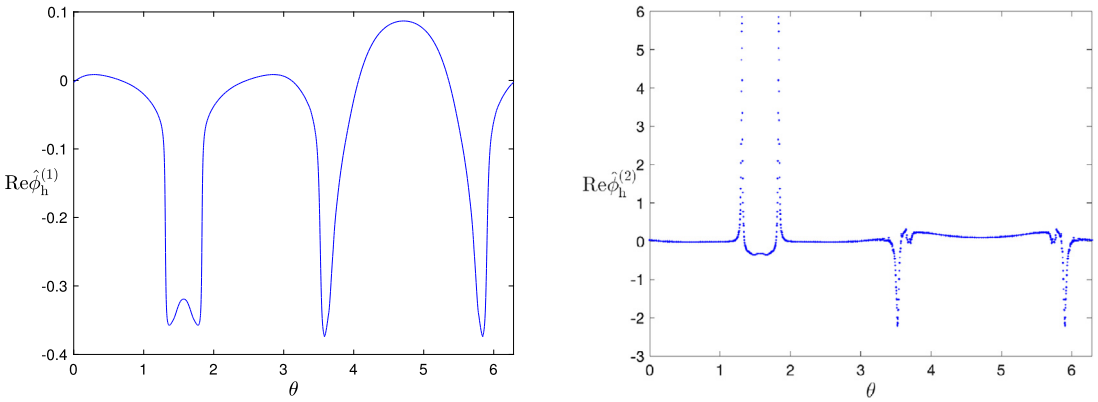

Fig. 5. The real parts of $\hat{\phi}_h^{(1)}$ and $\hat{\phi}_h^{(2)}$ obtained from the adaptive algorithm in Example 2. θ represents the polar angle over the ellipse.

errors are $\hat{e}^{(1)}=0.0044$ and $\hat{e}^{(2)}=0.0745$, respectively. As a comparison, if the mesh is quasi-uniform, one needs a much more refined mesh $\hat{\Gamma}_h$ with a total number of $2\bar{M}$ grid points to achieve a comparable accuracy, in which $\bar{M}=700$. This is illustrated in the last column of Table 1. In Fig. 4 we also plot the wave field in the domain Ω_1 and Ω_2, which are computed via the formulas (2.14) and (2.15) using the solutions $\hat{\phi}_h^{(1)}$ and $\hat{\phi}_h^{(2)}$ obtained from the adaptive algorithm. The preferential propagation of the wave in the hyperbolic medium and the multiple reflections by the interface Γ is clearly seen.

Example 2. The geometry in this example is the same as Example 1, but both media in Ω_1 and Ω_2 are now hyperbolic. Their permittivity values are given by $\varepsilon_1^{(1)}=-1+0.02i$, $\varepsilon_2^{(1)}=1+0.02i$, and $\varepsilon_1^{(2)}=-4+0.05i$, $\varepsilon_2^{(2)}=1+0.05i$. Assume that the source is located in exterior domain such that $f_1=0$ and $f_2=-\delta(x-x_0)$, in which the source location is $x_0=(0,2)$.

The adaptive procedure also terminates with $\ell=4$ and the mesh $\Gamma_h^{(4)}$ attains a total of 249 grids points as shown in Fig. 2 (right). The final numerical solutions $\hat{\phi}_h^{(1)}$ and $\hat{\phi}_h^{(2)}$ are plotted in Fig. 5, and the corresponding numerical errors are $\hat{e}^{(1)}=0.0034$ and $\hat{e}^{(2)}=0.0616$, respectively. For completeness, we collect all the mesh sizes and the corresponding numerical errors for different levels of refinements in Table 2. The computation with a quasi-uniform mesh to achieve a comparable accuracy is also shown. We see that the number of degrees of freedom is reduced by about 4 times when the adaptive procedure is applied. Fig. 6 demonstrates the wave field in the domain Ω_1 and Ω_2. The wave is strongly directional while penetrating through the interior hyperbolic medium and being reflected at the interface.

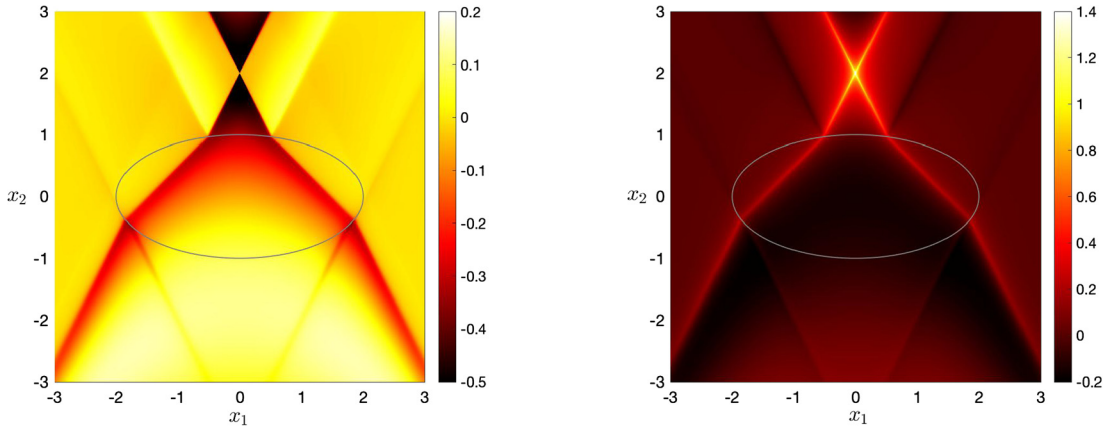

Fig. 6. Real (left) and imaginary part (right) of the wave field inside and outside the elliptical domain in Example 2.

Table 3
The maximum and minimum mesh sizes $h_{\max}$ and $h_{\min}$ for $\Gamma_h^{(\ell)}$, and the relative errors $\hat{e}^{(1)}$ and $\hat{e}^{(2)}$ for the adaptive BEM and non-adaptive BEM (Example 3).

	Adaptive BEM				Non-adaptive BEM
	$M^{(0)} = 120$	$M^{(1)} = 150$	$M^{(2)} = 190$	$M^{(3)} = 238$	$\bar{M} = 672$
$h_{\max}$	0.02	0.02	0.02	0.02	0.0036
$h_{\min}$	0.02	0.01	0.0050	0.0025	0.0036
$\hat{e}^{(1)}$	0.0333	0.0078	0.0023	0.0011	3.76×10^{-4}
$\hat{e}^{(2)}$	0.5684	0.2860	0.1268	0.0722	0.0714

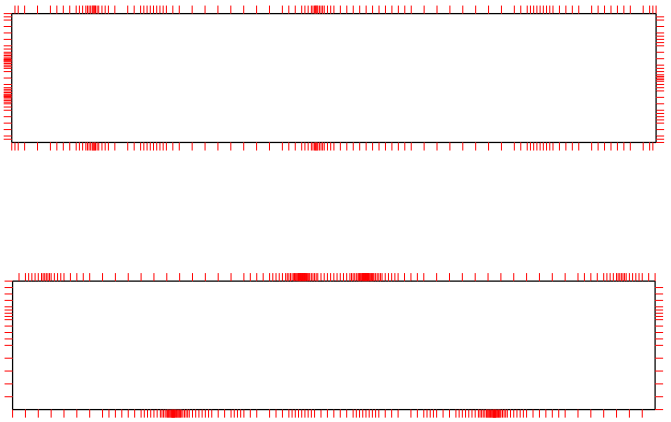

Fig. 7. The mesh $\Gamma_h^{(3)}$ (top) and $\Gamma_h^{(4)}$ (bottom) over the boundary of the rectangle for Example 3 and Example 4 respectively.

Example 3. In this example, we consider a rectangular hyperbolic slab placed in the vacuum. The permittivity values are $\varepsilon_1^{(1)} = 1 + 0.02i$, $\varepsilon_2^{(1)} = -3 + 0.1i$ in the rectangular domain $\Omega_1 = (0, 1) \times (0, 0.2)$. When the source is located at $(0.3, 0.1)$ and the wavenumber $k_0 = 1$, the mesh sizes and the corresponding numerical errors for the adaptive algorithm are shown in Table 3. Here we obtain the reference solutions $\phi^{(1)}$ and $\phi^{(2)}$ with high-order accuracy by using a uniform fine mesh with 12000 grid points. The final mesh $\Gamma_h^{(3)}$ attains a total of 238 grids points as shown in Fig. 7 (top). The numerical errors for the solutions obtained from $\hat{\Gamma}_h^{(3)}$ are $\hat{e}^{(1)} = 0.0011$ and $\hat{e}^{(2)} = 0.0722$, respectively. In contrast, the same level of accuracy is obtained by a quasi-uniform mesh $\hat{\Gamma}_h$ with a total number of $2\bar{M}$ grid points, in which $\bar{M} = 672$. Fig. 8 plots the wave field in the domain Ω_1 and Ω_2. It is observed that multiple reflections by the interface induce strong wave interactions inside Ω_1.

Example 4. We consider the same geometry as in Example 3 while assigning the permittivity values as $\varepsilon_1^{(1)} = -1 + 0.02i$, $\varepsilon_2^{(1)} = 1 + 0.02i$ and $\varepsilon_1^{(2)} = -4 + 0.05i$, $\varepsilon_2^{(2)} = 1 + 0.05i$ for the interior and exterior domain, respectively. The wavenumber $k_0 = 2\pi$, and the source is located in exterior domain with $f_1 = 0$ and $f_2 = -\delta(x - x_0)$, wherein the source location is

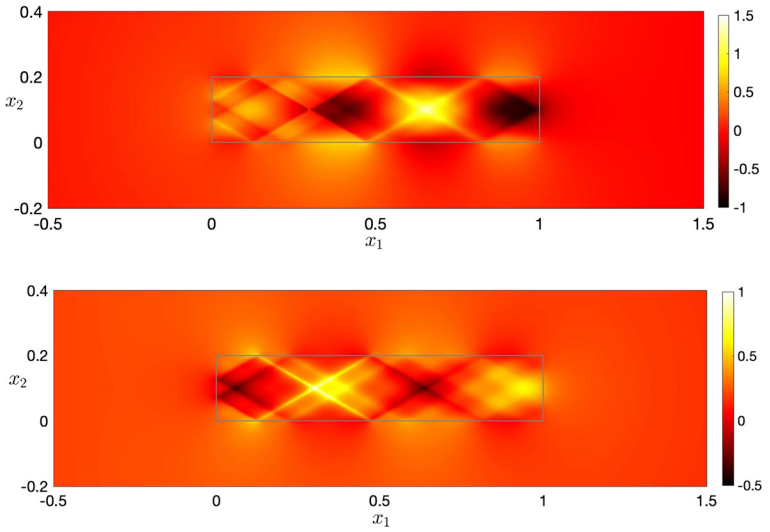

Fig. 8. Real (top) and imaginary part (bottom) of the wave field inside and outside the rectangle in Example 3.

Table 4
The maximum and minimum mesh sizes $h_{\max}$ and $h_{\min}$ for $\Gamma_h^{(\ell)}$, and the relative errors $\hat{e}^{(1)}$ and $\hat{e}^{(2)}$ for the adaptive BEM and non-adaptive BEM (Example 4).

	Adaptive BEM					Non-adaptive BEM
	$M^{(0)} = 120$	$M^{(1)} = 150$	$M^{(2)} = 188$	$M^{(3)} = 235$	$M^{(4)} = 294$	$\bar{M} = 1920$
$h_{\max}$	0.02	0.02	0.02	0.02	0.02	0.0013
$h_{\min}$	0.02	0.01	0.005	0.0025	1.25×10^{-3}	0.0012
$\hat{e}^{(1)}$	0.1044	0.0365	0.0093	0.0015	8.31×10^{-4}	7.79×10^{-4}
$\hat{e}^{(2)}$	0.7599	0.6673	0.4123	0.1785	0.0812	0.0804

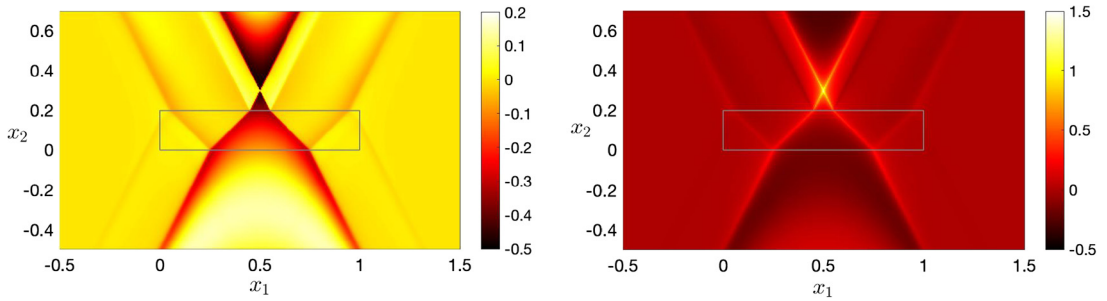

Fig. 9. Real (left) and imaginary part (right) of the wave field inside and outside the rectangle in Example 4.

$x_0 = (0.5, 0.3)$. The adaptive boundary element still successfully leads to a reduction of numerical errors to the desired accuracy when the mesh refinement is performed locally, as demonstrated by Table 4. Due to the singularity of the solution, one needs a quasi-uniform mesh with the mesh size $h_{max} = 0.0013$ to achieve an accuracy that is obtained by an adaptive mesh with $h_{max} = 0.02$. The number of degrees of freedom for the former is more than 5 times higher than the latter. The final mesh in the adaptive procedure and the corresponding wave field in the domain are shown in Figs. 7 (bottom) and 9, respectively.

Example 5. In the final example, the interior domain Ω_1 attains a wedge shape and it is placed in the vacuum. Such geometry has been be used for super-focusing of the electromagnetic waves near the sharp tip [33]. The permittivity values for the hyperbolic medium are $\varepsilon_1^{(1)} = 2$, $\varepsilon_2^{(1)} = -3 + 0.03i$. The source is located in Ω_1 so that $f_1 = -\delta(x - x_0)$ with $x_0 = (0.1, 0.1)$ and $f_2 = 0$, and the wavenumber $k_0 = 1$. Similar to Example 3, the reference solutions $\phi^{(1)}$ and $\phi^{(2)}$ are obtained with high-order accuracy by using a uniform mesh with more than 10000 grid points. The adaptive algorithm starts with $M^{(0)} = 220$ and terminates after three mesh refinements. The mesh $\Gamma_h^{(3)}$ over the wedge boundary is shown in Fig. 10. The final numerical solutions $\hat{\phi}_h^{(1)}$ and $\hat{\phi}_h^{(2)}$ attain an accuracy of $\hat{e}^{(1)} = 0.0030$ and $\hat{e}^{(2)} = 0.0658$ respectively

Table 5
The maximum and minimum mesh sizes $h_{\max}$ and $h_{\min}$ for $\Gamma_h^{(\ell)}$, and the relative errors $\hat{e}^{(1)}$ and $\hat{e}^{(2)}$ for the adaptive BEM and non-adaptive BEM (Example 5).

	Adaptive BEM				Non-adaptive BEM
	$M^{(0)} = 220$	$M^{(1)} = 275$	$M^{(2)} = 344$	$M^{(3)} = 431$	$\bar{M} = 1210$
$h_{\max}$	0.0102	0.0102	0.0102	0.0102	0.0019
$h_{\min}$	0.01	0.005	0.0025	1.25×10^{-3}	0.0018
$\hat{e}^{(1)}$	0.0219	0.0110	0.0051	0.0030	0.0062
$\hat{e}^{(2)}$	0.4025	0.2515	0.1126	0.0658	0.0696

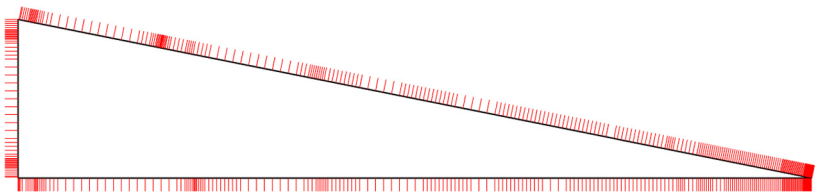

Fig. 10. The mesh $\Gamma_h^{(3)}$ over the boundary of the wedge in Example 5.

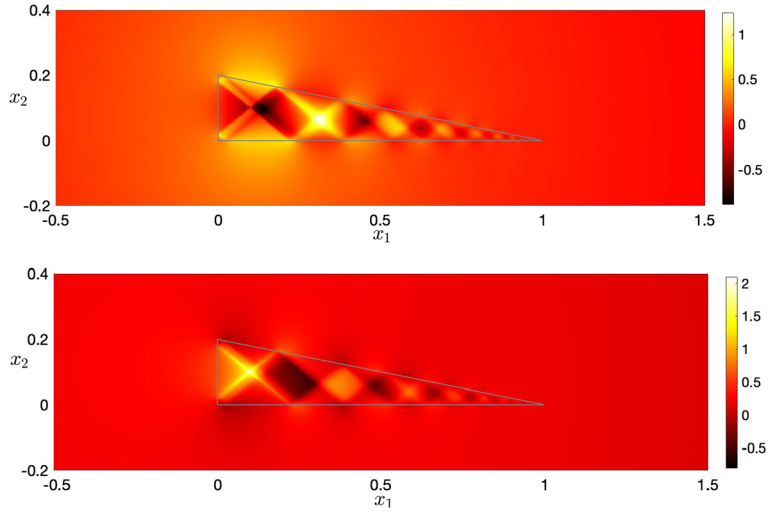

Fig. 11. Real (top) and imaginary part (bottom) of the wave field inside and outside the wedge in Example 5.

(see Table 5). As demonstrated in Fig. 11, the wave propagates toward the tip while being reflected by the boundary of the wedge.

5. Discussions

An adaptive boundary-integral equation method was presented in this paper for solving the transmission problem with hyperbolic metamaterials. Compared to the discretization with a quasi-uniform mesh, the adaptive approach is able to resolve the singular behavior of the solution with local mesh refinement, which reduces the number of the degrees of freedom and the overall computational cost significantly. There are several theoretical and computational issues to be explored along this direction. Although numerical examples show the efficacy of the error estimator and the accuracy of the adaptive procedure, the robust analysis of the estimator and the convergence analysis of the algorithm have not been carried out yet. As pointed out previously, this work is mainly on the demonstration of the adaptive algorithm for the two dimensional problems, its application in three dimensions has not been explored. It is expected that the adaptive algorithm would offer even larger reduction on the computational cost for 3D simulations. However, the computation becomes more challenging for mesh refinement and numerical integration in 3D. Note that for the full Maxwell's equations, the Dyadic Green's functions used in the integral formulation is highly anisotropic with coexistence of the cone-like pattern due to emission of the extraordinary TM-polarized waves and elliptical pattern due to emission of ordinary TE-polarized waves [35]. Finally, efficient integral equation methods for hyperbolic metamaterials with unbounded domains (e.g. layered media) and other settings of practical interest remain to investigated. The propagation nature of waves with arbitrarily large wave vectors inside the propagating cone requires new treatment in developing the computational algorithms.

CRediT authorship contribution statement

The single author Junshan Lin contributes solely to this work.

Declaration of competing interest

The authors declare that they have no known competing financial interests or personal relationships that could have appeared to influence the work reported in this paper.

References

[1] H. Ammari, H. Kang, B. Fitzpatrick, M. Ruiz, S. Yu, H. Zhang, Mathematical and Computational Methods in Photonics and Phononics, Mathematical Surveys and Monographs, vol. 235, American Mathematical Society, Providence, 2018.
[2] J. Berntsen, T. Espelid, A. Genz, An adaptive algorithm for the approximate calculation of multiple integrals, ACM Trans. Math. Softw. 17 (1991) 437–451.
[3] E. Bonnetier, H-M. Nguyen, Superlensing using hyperbolic metamaterials: the scalar case, J. Éc. Polytech., Math. 4 (2017) 973–1003.
[4] F. Bu, J. Lin, F. Reitich, A fast and high-order method for the three-dimensional elastic wave scattering problem, J. Comput. Phys. 258 (2014) 856–870.
[5] J. Caldwell, et al., Sub-diffractional volume-confined polaritons in the natural hyperbolic material hexagonal boron nitride, Nat. Commun. 5 (2014) 1–9.
[6] C. Carstensen, An a posteriori error estimate for a first-kind integral equation, Math. Comput. 66 (1997) 139–155.
[7] C. Carstensen, B. Faermann, Mathematical foundation of a posteriori error estimates and adaptive mesh-refining algorithms for boundary integral equations of the first kind, Eng. Anal. Bound. Elem. 25 (2001) 497–509.
[8] C. Carstensen, M. Maischak, D. Praetorius, E.P. Stephan, Residual-based a posteriori error estimate for hypersingular equation on surfaces, Numer. Math. 97 (2004) 397–425.
[9] C. Carstensen, D. Praetorius, Averaging Techniques for a Posteriori Error Control in Finite Element and Boundary Element Analysis, Lect. Notes Appl. Comput. Mech., vol. 29, Springer, Berlin, 2007.
[10] W. Chew, J. Jin, E. Michielssen, J. Song, Fast and Efficient Algorithms in Computational Electromagnetics, Artech House, 2001.
[11] W. Chew, M. Tong, B. Hu, Integral equation methods for electromagnetic and elastic waves, in: Synthesis Lectures on Computational Electromagnetics, 2008.
[12] D. Colton, R. Kress, Integral Equation Methods in Scattering Theory, Society for Industrial and Applied Mathematics, 2013.
[13] C. Cortes, W. Newman, S. Molesky, Z. Jacob, Quantum nanophotonics using hyperbolic metamaterials, J. Opt. 14 (2012) 063001.
[14] M. Costabel, E. Stephan, A direct boundary integral equation method for transmission problems, J. Math. Anal. Appl. 106 (1985) 367–413.
[15] M. Costabel, E. Stephan, Integral equations for transmission problems in linear elasticity, J. Integral Equ. Appl. 2 (1990) 211–223.
[16] S. Dai, et al., Tunable phonon polaritons in atomically thin van der Waals crystals of boron nitride, Science 343 (2014) 1125–1129.
[17] S. Dai, et al., Subdiffractional focusing and guiding of polaritonic rays in a natural hyperbolic material, Nat. Commun. 6 (2015) 1–7.
[18] B. Faermann, Local a-posteriori error indicators for the Galerkin discretization of boundary integral equations, Numer. Math. 79 (1998) 43–76.
[19] B. Faermann, Localization of the Aronszajn-Slobodeckij norm and application to adaptive boundary element methods. I. The two-dimensional case, IMA J. Numer. Anal. 20 (2000) 203–234.
[20] M. Feischl, et al., Adaptive boundary element methods, Arch. Comput. Methods Eng. 22 (2015) 309–389.
[21] L. Ferrari, et al., Hyperbolic metamaterials and their applications, Prog. Quantum Electron. 40 (2015) 1–40.
[22] S. Ferraz-Leite, C. Ortner, D. Praetorius, Convergence of simple adaptive Galerkin schemes based on $h - h/2$ error estimators, Numer. Math. 116 (2010) 291–316.
[23] S. Ferraz-Leite, D. Praetorius, Simple a posteriori error estimators for the h-version of the boundary element method, Computing 83 (2008) 135–162.
[24] W. Gander, W. Gautschi, Adaptive quadrature - revisited, BIT Numer. Math. 40 (2000) 84–101.
[25] L. Greengard, V. Rokhlin, A fast algorithm for particle simulations, J. Comput. Phys. 73 (1987) 325–348.
[26] Y. Guo, C. Cortes, S. Molesky, Z. Jacob, Broadband super-Planckian thermal emission from hyperbolic metamaterials, Appl. Phys. Lett. 101 (2012) 131106.
[27] G. Hsiao, W. Wendland, Boundary Integral Equations, Applied Mathematical Sciences, vol. 164, Springer-Verlag, 2008.
[28] Z. Jacob, L. Alekseyev, E. Narimanov, Optical hyperlens: far-field imaging beyond the diffraction limit, Opt. Express 14 (2006) 8247–8256.
[29] R. Kleinman, P. Martin, On single integral equations for the transmission problem of acoustics, SIAM J. Appl. Math. 48 (1988) 307–325.
[30] R. Kress, Linear Integral Equations, Applied Mathematical Sciences, vol. 82, Springer, Berlin, 1989.
[31] W. Ma, et al., In-plane anisotropic and ultra-low-loss polaritons in a natural van der Waals crystal, Nature 562 (2018) 557–562.
[32] J.C. Nédélec, Acoustic and Electromagnetic Equations: Integral Representations for Harmonic Problems, Applied Mathematical Sciences, vol. 144, Springer Science & Business Media, 2013.
[33] A. Nikitin, et al., Nanofocusing of hyperbolic phonon polaritons in a tapered boron nitride slab, ACS Photonics 3 (2016) 924–929.
[34] K. Novoselov, O. Mishchenko, O.A. Carvalho, A. Castro, Neto, 2D materials and van der Waals heterostructures, Science 353 (2016) 6298.
[35] A. Potemkin, A. Poddubny, P. Belov, Y. Kivshar, Green function for hyperbolic media, Phys. Rev. A 86 (2012) 023848.
[36] A. Poddubny, I. Iorsh, P. Belov, Y. Kivshar, Hyperbolic metamaterials, Nat. Photonics 7 (2013) 948–957.
[37] A. Salandrino, N. Engheta, Far-field subdiffraction optical microscopy using metamaterial crystals: theory and simulations, Phys. Rev. B 74 (2006) 075103.
[38] K. Sreekanth, et al., Extreme sensitivity biosensing platform based on hyperbolic metamaterials, Nat. Mater. 15 (2016) 621–627.
[39] P. Shekhar, J. Atkinson, Z. Jacob, Hyperbolic metamaterials: fundamentals and applications, Nano Converg. 1 (2014) 1–17.
[40] J. Taboada-Gutiérrez, et al., Broad spectral tuning of ultra-low-loss polaritons in a van der Waals crystal by intercalation, Nat. Mater. 19 (2020) 964–968.
[41] W. Wendland, D. Yu, Adaptive boundary element methods for strongly elliptic integral equations, Numer. Math. 53 (1988) 539–558.